OXFORD

Cerebral Cortex, 2022, **32**, 4492–4501
https://doi.org/10.1093/cercor/bhab497
Advance access publication date 2 February 2022
Original Article

Laminar-specific functional connectivity mapping with multi-slice line-scanning fMRI

Sangcheon Choi[1,2], Hang Zeng[1,2], Yi Chen[1], Filip Sobczak[1,2], Chunqi Qian[3]* and Xin Yu[4,]*

[1]Department of High-field Magnetic Resonance, Max Planck Institute for Biological Cybernetics, Tübingen 72076, Germany,
[2]Graduate Training Centre of Neuroscience, University of Tübingen, Tübingen 72074, Germany,
[3]Department of Radiology, Michigan State University, East Lansing, MI 48824, USA,
[4]Athinoula A. Martinos Center for Biomedical Imaging, Department of Radiology, Harvard Medical School, Massachusetts General Hospital, Charlestown, MA 02129, USA

*Address correspondence to Dr Xin Yu, 149, 13th Street, Charlestown, MA 02129, USA. Email: xyu9@mgh.harvard.edu; Dr Chunqi Qian, 846 Service Rd, East Lansing, MI 48824, USA. Email: qianchu1@msu.edu

Despite extensive studies detecting laminar functional magnetic resonance imaging (fMRI) signals to illustrate the canonical microcircuit, the spatiotemporal characteristics of laminar-specific information flow across cortical regions remain to be fully investigated in both evoked and resting conditions at different brain states. Here, we developed a multislice line-scanning fMRI (MS-LS) method to detect laminar fMRI signals in adjacent cortical regions with high spatial (50 μm) and temporal resolution (100 ms) in anesthetized rats. Across different trials, we detected either laminar-specific positive or negative blood-oxygen-level-dependent (BOLD) responses in the surrounding cortical region adjacent to the most activated cortex under the evoked condition. Specifically, in contrast to typical Layer (L) 4 correlation across different regions due to the thalamocortical projections for trials with positive BOLD, a strong correlation pattern specific in L2/3 was detected for trials with negative BOLD in adjacent regions, which indicated brain state-dependent laminar-fMRI responses based on corticocortical interaction. Also, in resting-state (rs-) fMRI study, robust lag time differences in L2/3, 4, and 5 across multiple cortices represented the low-frequency rs-fMRI signal propagation from caudal to rostral slices. In summary, our study provided a unique laminar fMRI mapping scheme to better characterize trial-specific intra- and inter-laminar functional connectivity in evoked and resting-state MS-LS.

Key words: BOLD; cortical layer; functional connectivity; laminar fMRI; resting-state fMRI.

Introduction

Resting-state (rs-) functional magnetic resonance imaging (fMRI) is widely utilized in clinical and cognitive neuroscience for functional connectivity mapping, attributing to its unique capability to identify low-frequency oscillation arised from neuronal oscillation across different brain states (Biswal et al. 1995; Fox and Raichle 2007; Biswal et al. 2010; Biswal 2012; Buckner et al. 2013). The conventional method of rs-fMRI is based on echo-planar-imaging (EPI) to detect T2∗-weighted blood-oxygen-level-dependent (BOLD) signal low-frequency fluctuation across functionally connected brain regions (Turner et al. 1991). This mapping method has been increasingly utilized to parcellate functional networks across the whole brain (Beckmann et al. 2005; Smith et al. 2009, 2013; Yeo et al. 2011; Preibisch et al. 2015; Sobczak et al. 2021). Lately, high-field fMRI has also been utilized in the mapping scheme to identify dynamic BOLD responses and cerebral blood volume (CBV) signals with layer specificity in bottom-up or top-down tasks (Silva and Koretsky 2002; Goense and Logothetis 2006; Huber et al. 2017; Kashyap et al. 2018; Finn et al. 2019; Sharoh et al. 2019; Yu et al. 2019), indicating the possible functional network across different cortical layers. However, the spatial resolution of fMRI images is often limited by the demanding requirement for high temporal resolution, that is, fast-sampling of rs-fMRI oscillation patterns, at subsecond with sufficient signal-to-noise ratio (SNR) (Lewis et al. 2016; Agrawal et al. 2020; Gil et al. 2021). In addition, potential aliasing effects from the cardiorespiratory artifacts (Birn et al. 2006; Murphy et al. 2013; Pais-Roldan et al. 2018) contaminate fMRI signals, leading to spurious results for rs-fMRI studies without sufficient sampling rates. It remains challenging to achieve high spatial resolution with a fast sampling rate to acquire rs-fMRI signals with sufficient SNR for brain functional mapping.

Previously, Yu et al. have developed a line-scanning fMRI method to substantially improve spatiotemporal resolution in rat brains, μ achieving 50-μm spatial

Received: March 25, 2021. **Revised:** November 30, 2021. **Accepted:** December 1, 2021

resolution along a line profile which covers different cortical layers within 50-ms TR (Yu et al. 2014). Line-scanning fMRI has also been used in combination with fiber-based optogenetic stimulation (Albers et al. 2018) or diffusion-sensitizing gradients (Nunes et al. 2021) to study the fast functional onset with high temporal resolution. Beyond preclinical studies, line-scanning fMRI is also being utilized in human fMRI studies to provide functional maps of cortical layers in a reduced field-of-view (FOV) with high spatiotemporal resolution (Raimondo et al. 2019; Siero et al. 2019; Morgan et al. 2020). Lately, a similar line-scanning strategy has been used to map diffusion signals in the human brain (Balasubramanian et al. 2021). To date, however, no fMRI measurements have been performed on multiple cortical regions manifesting laminar-specific functional connectivity with high spatiotemporal resolution comparable to the original line-scaninng fMRI method.

In this study, we extended the line-scanning fMRI method toward multislice acquisition to acquire line profiles from different cortical regions (Choi et al. 2021) with high spatial (50 μm) and temporal (100 ms) resolution. To investigate functional connectivity driven by the underlying neural network, we analyzed the intra- and inter-laminar correlation features under both evoked and resting-state conditions in anesthetized rats. Upon electrical stimulation of the forepaw, adjacent cortical regions to the forepaw somatosensory cortex (FP-S1) showed either positive or negative BOLD responses with distinct laminar-specific correlation patterns across different fMRI trials. Meanwhile, owing to the fast sampling rate, we were able to detect laminar-specific lag times of rs-fMRI signals with low-frequency fluctuation, showing specific signal propagation (< 0.1 Hz) across different cortices. Our work demonstrates the feasibility of multislice line-scanning fMRI (MS-LS) to identify evoked laminar correlation patterns and resting-state signal propagation across different cortical regions.

Materials and Methods

Animal Preparation

The study was performed in accordance with the German Animal Welfare Act (TierSchG) and Animal Welfare Laboratory Animal Ordinance (TierSchVersV), in full compliance with the guidelines of the EU Directive on the protection of animals used for scientific purposes (2010/63/EU). The study was reviewed by the ethics commission (§15 TierSchG) and approved by the state authority (Regierungspräsidium, Tübingen, Baden-Württemberg, Germany). A 12–12 hour on/off lighting cycle was maintained to assure undisturbed circadian rhythm. Food and water were obtainable ad libitum. A total of 4 male Sprague–Dawley rats were used in this study.

Anesthesia was first induced in the animal with 5% isoflurane in the chamber. The anesthetized rat was intubated using a tracheal tube. A mechanical ventilator (SAR-830, CWE, USA) was used to ventilate animals throughout the whole experiment. Femoral arterial and venous catheterization was performed with polyethylene tubing for blood sampling, drug administration, and constant blood pressure measurements. After the surgery, isoflurane was switched off, and a bolus of the anesthetic alpha-chloralose (80 mg/kg) was infused intravenously. After the animal was transferred to the MRI scanner, a mixture of alpha-chloralose (26.5 mg/kg/h) and pancuronium (2 mg/kg/h) was constantly infused to maintain the anesthesia level for reduced motion artifacts.

EPI fMRI Acquisition

All data sets from rats were acquired using a 14.1 T/26 cm (Magnex, Oxford) horizontal bore magnet with an Avance III console (Bruker, Ettlingen) and a 12-cm diameter gradient system (100 G/cm, 150 μs rising time). A home-made transceiver surface coil with 20-mm diameter was used on the rat brain in all experiments. For the functional map of BOLD activation (Fig. 1A) (Choi et al. 2020), a 3D gradient-echo EPI sequence was acquired with the following parameters: TR/TE 1500/11.5 ms, FOV $1.92 \times 1.92 \times 1.92$ cm^3, matrix size $48 \times 48 \times 48$, spatial resolution $0.4 \times 0.4 \times 0.4$ mm^3. A high order (e.g., 2nd or 3rd order) shimming was applied to reduce the main magnetic field (B0) inhomogeneities at the region-of-interest (ROI). For anatomical reference of the activated BOLD map, a RARE sequence was applied to acquire 48 coronal images with the same geometry as that of the EPI images. The fMRI design paradigm for each trial comprised 200 dummy scans to reach steady-state, 10 prestimulation scans, 3 scans during stimulation, and 12 poststimulation scans with a total of 8 epochs.

MS-LS Acquisition

GRE-based MS-LS data sets were acquired with a 6-mm diameter home-made transceiver surface coil in anesthetized rats for evoked and rs-fMRI. The MS-LS method was applied by increasing the slice dimension (1–3) to record fMRI signals in three different cortical regions covering FP-S1 (i.e. rostral, middle, and caudal cortices) and using two saturation slices to avoid aliasing artifacts along the phase-encoding direction (Fig. 1A). Two saturation slices were applied once before the first slice within one TR for three slice MS-LS acquisition. To compare the performance of the saturation slices across three different slices, 2D profiles from three different cortical regions were acquired (see Supplementary Fig. S1A). The phase-encoding gradient was turned off to acquire line profiles (Fig. 1C). Laminar-specific fMRI responses from the three cortices were acquired along the frequency-encoding direction with 50-μm spatial resolution. The following acquisition parameters were used: TR/TE 100/9 ms, TA 10 min 40 s, FA 50°, slice thickness 1.2 mm, slice gap 1.5 mm, FOV 6.4×1.2 mm^2, and matrix 128×32. The fMRI design paradigm for each epoch consisted of 1 s prestimulation, 4 s stimulation,

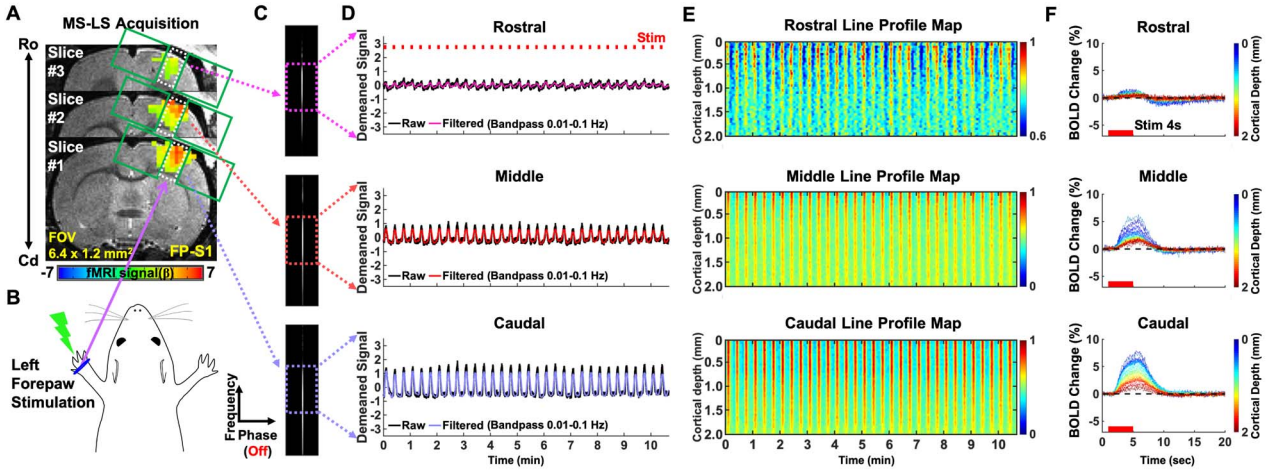

Fig. 1. Evoked BOLD responses using the MS-LS method. (*A*) Schematic of the multilaminar line-scanning experimental design on EPI-BOLD activation maps of different cortical regions overlaid on anatomical RARE images. Three different regions (white boxes) between two saturation slices (green boxes) were targeted from a rostral (Ro) to a caudal (Cd) region covering FP-S1 of one hemisphere. (*B*) Left forepaw electrical stimulation (3 Hz, 4 s, 2.5 mA) following an fMRI design paradigm (1 s off, 4 s on, and 15 s off). (*C*) Representative three different line-scanning profiles from the corresponding slices. Each colored box indicates the corresponding cortical region. (*D*–*F*) Average results from all data sets ($n = 18$ trials of 4 rats). (*D*) Demeaned fMRI time series of raw (black) and filtered (magenta, orange, light purple, bandpass: 0.01–0.1 Hz) data (average of 40 voxels) in the rostral (upper), middle (middle), and caudal (lower) cortical regions under the evoked condition. Red boxes indicate 32 epochs for 10 min 40 s. (*E*) Normalized line profile maps showing the laminar-specific fMRI responses across the cortical depth (0–2 mm) in the three cortical regions (40 voxels with 50 μm resolution). The time courses were processed by band-pass filtering (0.01–0.1 Hz). (*F*) Average BOLD changes of the individual voxel time courses (mean epoch with 20 s) across the cortical depth in the three cortical regions.

and 15 s poststimulation for a total of 20 s. Around 40 dummy scans were performed at the beginning of each trial to reach a steady state. A total of 6400 lines (i.e. 10 min 40 s, 32 epochs per evoked trial) in each cortex were acquired in every single trial for evoked and rs-fMRI. A total of 18 trials in evoked fMRI and 18 trials in rs-fMRI were acquired from 4 rats. Evoked BOLD activation was identified by performing electrical stimulation to the left forepaw (300 μs duration at 2.5 mA repeated at 3 Hz for 4 s).

Data Analysis

All signal processing and analyses were implemented in MATLAB software (Mathworks, Natick, MA) and Analysis of Functional NeuroImages software (Cox 1996) (AFNI, NIH, USA). For evoked fMRI analysis in Figure 1A and Supplementary Figure S2, the hemodynamic response function (HRF) was the default of the block function of the linear program "3dDeconvolve" in AFNI. BLOCK (L, 1) computes a convolution of a square wave of duration L and makes a peak amplitude of block response = 1, with $g(t) = t^4e^{-t}/[4^4e^{-4}]$. Each beta weight represents the peak height of the corresponding BLOCK curve for that class. The HRF model is defined as follows:

$$\mathrm{HRF}(t) = \mathbf{int}\left(g\left(t - s\right), s = 0..\mathbf{min}\left(t, L\right)\right)$$

Cortical surfaces were determined based on signal intensities of fMRI line profiles (Fig. 1C). The detailed processing procedure was conducted as described in the previous line-scanning study (Yu et al. 2014). For Figures 1D and 3A, demeaned fMRI time courses were used as follows: (x—μ), where x was the original fMRI time courses and μ was the mean of the time courses. The line profile map concatenated with multiple line-scanning fMRI profiles was normalized by its maximum intensity. Average BOLD time series and percentage changes were defined as (S − S0)/S0 × 100%, where S was the BOLD signal and S0 was the baseline. S0 was obtained by averaging the fluctuation signal in the 1-s prestimulation window in evoked fMRI that was repeated every 20 s with the whole time series (640 s). The BOLD time series in each ROI were detrended ("polyfit" function in Matlab, order: 3) and bandpass filtered (0.01–0.1 Hz, FIR filter, order: 4096) before analyzing line profile maps, correlation coefficients, power spectral densities (PSDs), and cross-correlation. The bandpass filtering was performed as a zero-phase filter by "fir1" and "filter" functions in Matlab, compensating a group delay ("grpdelay" and "circshift" functions in Matlab) introduced by the FIR filter.

Temporal correlation analysis which is generally accepted as an indicator of corticocortical functional interaction, for example, increased correlation is thought to reflect increased functional connectivity between two brain sites (Bandettini et al. 1993; Friston 2011). In this study, the correlation analysis was used as an important indicator of laminar-specific functional connectivity across multiple cortical regions. Laminar-specific fMRI time courses were used and converted to the bandpass filtered time courses. The correlation is defined as follows:

$$\mathrm{Corr}_{xy}\left(a, b\right) = \frac{\sum_{i=1}^{n}\left(x_{a,i} - \overline{x}_a\right)\left(y_{b,i} - \overline{y}_b\right)}{\sqrt{\sum_{i=1}^{n}\left(x_{a,i} - \overline{x}_a\right)^2 \sum_{i=1}^{n}\left(y_{b,i} - \overline{y}_b\right)^2}}$$

where x, y indicates filtered fMRI time series (n time points), and a, b indicates a voxel from one cortical region. The correlation was calculated by "corr" function in MATLAB (Type: Pearson, Rows: pairwise). Fisher-Z transform was applied prior to averaging the correlation coefficients with multiple trials (Silver and Dunlap 1987). Temporal signal-to-noise ratio (tSNR) values were calculated across the cortical depths and different cortical regions to compare differences between correlation coefficients and tSNR values (see Supplementary Fig. S3).

For resting-state PSD analysis, fMRI time series was converted to the Z-score normalized time series. Subsequently, the converted time series was used to compare the frequency responses among the different regions avoiding the dependency of the difference in signal amplitudes (Fig. 3C). The Z-score normalized time courses were calculated as follows: $(x - \mu)/\sigma$, where x was original fMRI time courses and μ, σ were the mean and the standard deviation of the time courses, respectively ("zscore" function in Matlab). PSDs were calculated by Welch's estimation method ("pwelch" function in MATLAB, FFT length: 2000, overlap: 50%).

For lag time calculation in rs-fMRI, voxel-wise lag times were calculated by analyzing cross-correlation coefficients across all cortical layers or across different cortical regions ("xcorr" function in MATLAB). One laminar-specific lag time was determined as the time point with the maximal cross-correlation coefficient (Fig. 3D and E). The boundaries of different cortical layers were determined as provided in the previous line-scanning study (Yu et al. 2014).

For statistical analysis in evoked and rs-fMRI, one-way analysis of variance (ANOVA) tests (Figs 2E, G and 3D, E) were performed to compare laminar-specific values using the posthoc test with multiple trials across cortical layers, and to determine whether there were statistically significant differences among the associated population means in different cortical layers or areas. For evoked fMRI, Fisher-Z transform was applied before testing one-way ANOVA to meet the model assumption (i.e. normal distribution). For permutation tests in evoked fMRI and rs-fMRI (see Supplementary Figs S4, S5, and S6), we have performed permutation tests with laminar-specific time courses (e.g., L1 and L2/3, L1 and L4) of representative trials to determine statistical significances within correlation matrices. The repeated number (N) for the randomized sampling of the permutation tests was 1000. All trials were sorted into positive and negative BOLD groups (see Supplementary Fig. S7A) based on a peak polarity of average BOLD time courses in rostral cortical regions after stimulation (see Supplementary Fig. S8B). For example, if a peak of average BOLD time courses was below zero, one trial was sorted into the negative BOLD group. The Student's t-test was performed with the positive and negative BOLD groups (see Supplementary Fig. S7B). The P-values < 0.05 were considered statistically significant.

Results

Mapping Evoked Laminar-Specific BOLD Signals with Multislice Line-Scanning fMRI

We first developed the MS-LS method (Fig. 1A) to map laminar-specific BOLD responses from different cortical regions covering FP-S1 and adjacent cortices in one hemisphere (Yu et al. 2014) (for details, see the Method section). Left forepaw stimulation (Fig. 1B) activated contralateral cortical FP-S1, which has been reliably identified by using the conventional EPI method (Fig. 1A and Supplementary Fig. S2; negative BOLD) (Nair and Duong 2004; Kim et al. 2010; Wang et al. 2018; Jung et al. 2019). As shown in Figure 1C, three different line-scanning profiles from the corresponding cortical regions (i.e. rostral, middle, and caudal slices) were acquired by switching off phase-encoding gradient and defining the FOV with two saturation slices to avoid aliasing from regions outside the FOV (Fig. 1A). Evoked BOLD–fMRI signals in three slices were simultaneously recorded as a function of time across the cortical depth (0–2 mm), showing the most salient BOLD responses in the caudal slice with decreased BOLD signals from the middle to the rostral slice as shown in Figure 1D–F.

Distinguishing the Inter- and Intra-Laminar Functional Connectivity Across Different Cortices

Besides the typical positive BOLD signal detected in FP-S1 and adjacent area upon stimulation (Kim et al. 2010; Yu et al. 2014; Albers et al. 2018), negative BOLD signals were also reported in the adjacent cortex of activated regions (Hu et al. 1997; Devor et al. 2007; Boorman et al. 2010; Goense et al. 2012; de la Rosa et al. 2021). We applied MS-LS to characterize the laminar-specific correlation patterns of varied BOLD signals in cortical areas adjacent to activated FP-S1. As shown in Figure 2A, highly varied BOLD responses in the rostral slice were observed across all trials with left forepaw stimulation. We sorted individual trials into two groups based on BOLD responses of the rostral slice, showing group 1 with positive and group 2 with negative BOLD signals (Fig. 2A, Supplementary Figs S7 and S8). Figure 2B shows the laminar-specific BOLD responses across the three different slices for both groups. The spreading negative BOLD responses were observed at the superficial layers in the rostral slice and salient undershoot of the BOLD signal was detected in the middle slice in group 2 in contrast to the monophasic positive BOLD responses across the three slices in group 1. This result demonstrates that distinct BOLD responses in adjacent cortices to activated FP-S1 can be specified by MS-LS with laminar specificity.

Next, the intra- and inter-laminar correlation maps (Fig. 2C) were calculated to obtain group-averaged results. In the 3 × 3 matrix (Fig. 2D and F), the intralaminar correlation maps were arranged on the diagonal blocks, while the interlaminar correlation maps (i.e. rostral-middle, rostral-caudal, and middle-caudal correlation maps) were arranged on the off-diagonal blocks.

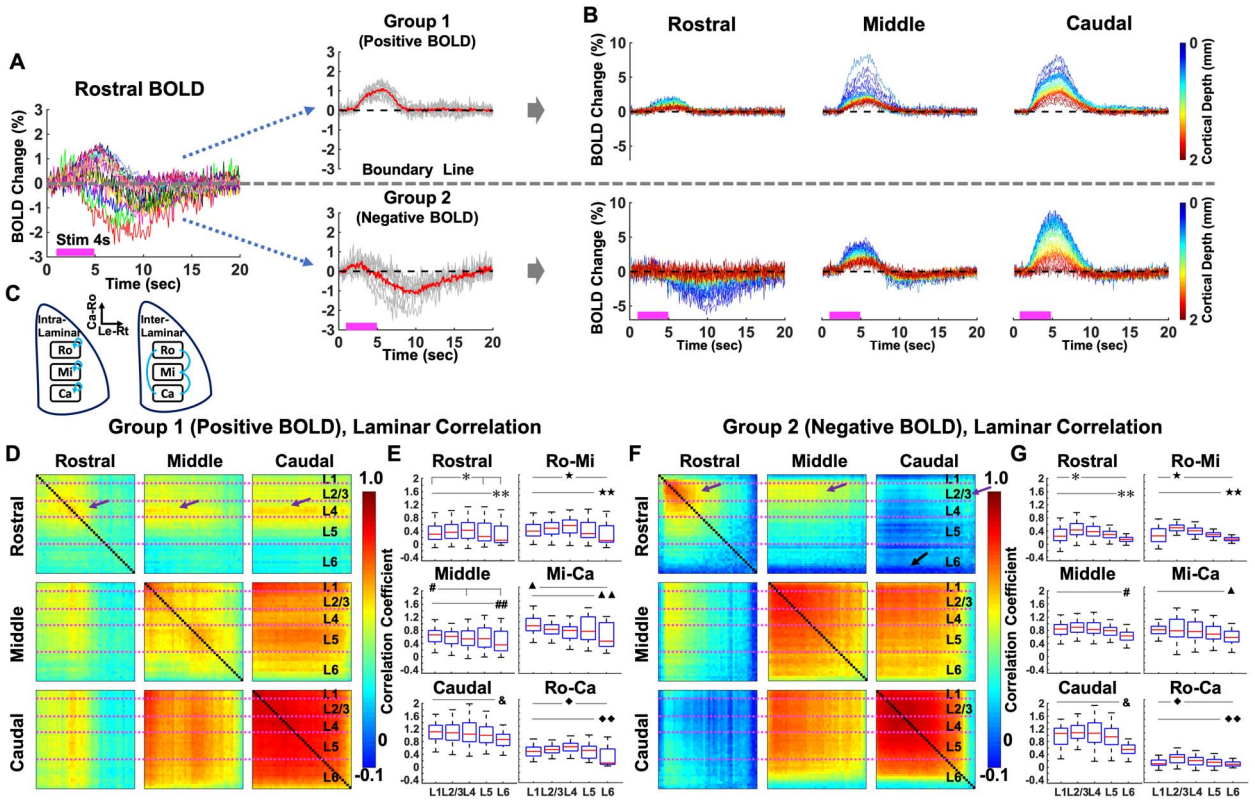

Fig. 2. (*A*) *Left*: Average BOLD changes (every 20 s) of the average voxel time series (average of 40 voxels) showing both positive and negative BOLD responses in the rostral region with different trials ($n = 18$ trials of 4 rats). The individual colors represent individual trials. *Right*: Grouping based on either the positive or negative BOLD response in the rostral region. Group 1 (11 trials) has positive BOLD, and group 2 (7 trials) has negative BOLD. (*B*) Three different average BOLD time series across the cortical depth (0–2 mm, 40 lines) in the rostral, middle, and caudal regions of group 1 and 2. (*C*) Schematic of intra- and inter-laminar correlation among the three cortical regions. (*D*–*G*) Group-averaged results representing intra- and inter-laminar correlation maps in group 1 (*D* and *E*) and group 2 (*F* and *G*). In a 3 × 3 matrix (*D* and *F*), diagonal and off-diagonal blocks represent intra- and inter-laminar correlation maps, respectively. L4 in group 1 and L2/3 in group 2 has higher correlation coefficients across the different cortical regions (purple arrows), showing significant differences (*E* and *G*) among all the layers. L6 shows significant difference in both groups while some parts of L6 in group 2 have negative correlation (*F*, black arrow). All statistic tests were performed with one-way ANOVA (posthoc: $P < 0.05$, Bonferroni correction).

From the intralaminar correlation analysis, higher correlation coefficients were observed in superficial layers over deep layers of caudal and middle slices in both groups, but the rostral slice showed stronger correlation at Layer (L) 4 in group 1 versus L2/3 in group 2 (Fig. 2*E* and *G*). Also, the interlaminar correlation coefficients in group 1 showed higher values in L4 over other layers, presumably presenting robust BOLD signal correlation of FP-S1 through thalamocortical projections (Yu et al. 2014; Bopp et al. 2017; El-Boustani et al. 2020). In contrast, the correlation coefficients for Ro-Mi and Ro-Ca in group 2 showed higher values in L2/3, possibly presenting a negative BOLD signal-dominated correlation through corticocortical projection-mediated lateral inhibition (Butovas and Schwarz 2003; Butovas et al. 2006; Thomson and Lamy 2007; Devor et al. 2007; Kunori and Takashima 2016). Moreover, the histograms of the permutation tests with laminar-specific time courses (e.g., L1 and L2/3, L1 and L4, etc.) of a representative trial demonstrated that the correlation values were statistically significant (see Supplementary Figs S4 and S5). The tSNR profiles in the different cortical regions (see Supplementary Fig. S3C) showed similar means and standard deviations and similar profiles (e.g., the highest tSNR in middle layers) on different cortical depths and regions while the corresponding correlation matrices showed largely varied correlation coefficients across the cortical depths and regions, indicating the laminar-specific correlation features were not merely driven by their tSNR values. Taken together, these results demonstrate distinct layer-specific correlation features underlying the positive and negative BOLD at the cortical areas adjacent to activated FP-S1, indicating brain state-dependent laminar fMRI responses across different trials.

Mapping the Laminar-Specific Functional Connectivity in rs-fMRI

The MS-LS method could also be used to investigate the laminar-specific correlation features of rs-fMRI signals from the different cortial regions. Figure 3*A* shows representative Z-score normalized time courses (average of 40 voxels) from the rostral, middle, and caudal slices, as well as the 2D line profile rs-fMRI maps as a function of time across the cortical depth, specifically presenting a highly synchronized slow oscillatory pattern. Figure 3*B*

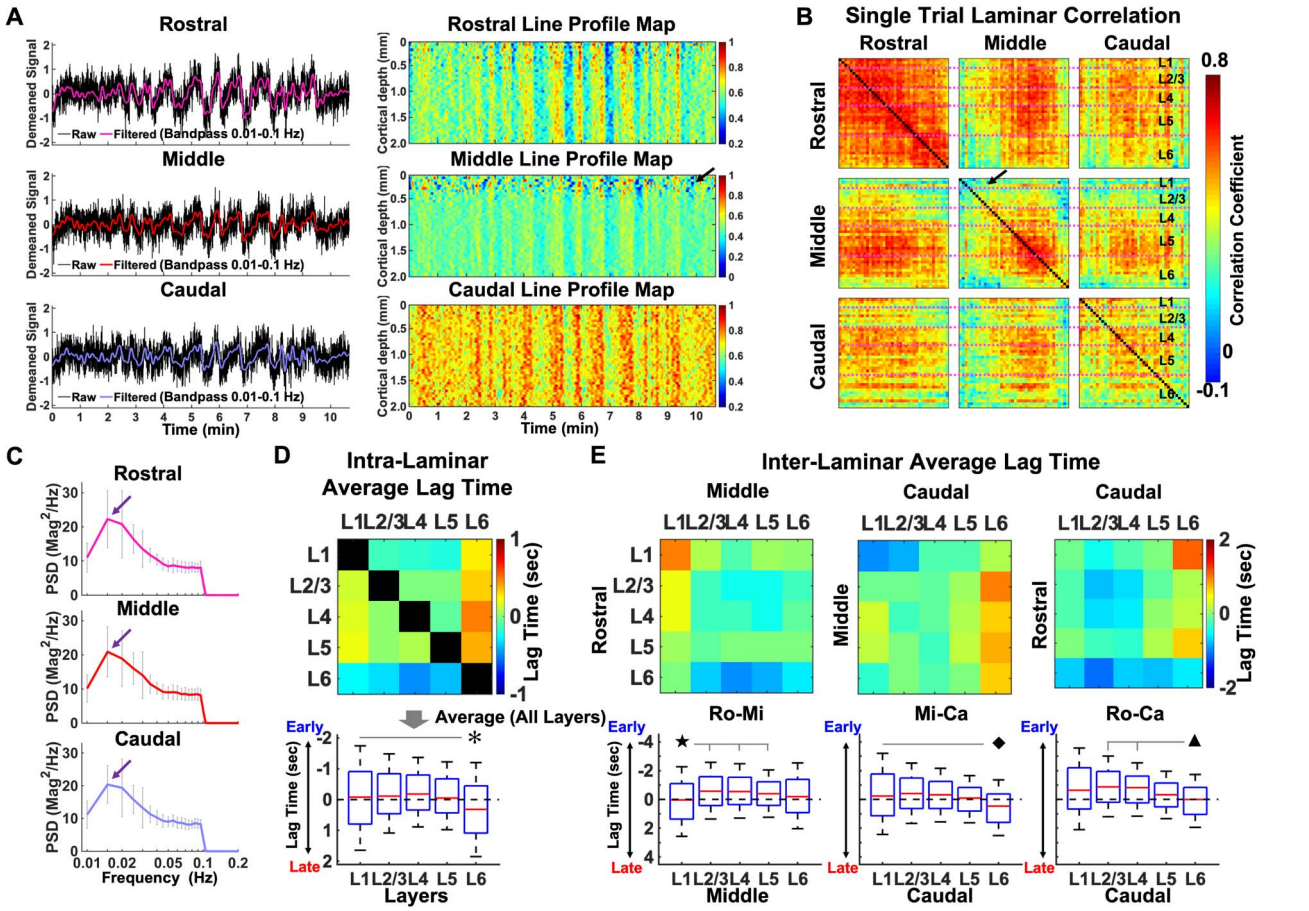

Fig. 3. (*A*) *Left*: Demeaned rs-fMRI time series of raw and filtered (bandpass: 0.01–0.1 Hz) data (average of 40 voxels) in rostral (upper), middle (middle), and caudal (lower) cortical regions from one representative trial (10 min 40 s). *Right*: Normalized line profile maps showing the laminar-specific responses across the cortical depth (0–2 mm, 40 voxels) in the three different regions. The maps were processed by band-pass filtering (0.01–0.1 Hz). (*B*) Laminar-specific correlation maps from the same trial in (*A*). In a 3 × 3 matrix, diagonal and off-diagonal blocks represent intra- and inter-laminar correlation maps, respectively. The black arrows (*A* and *B*) in the middle region indicate the BOLD effects of large draining veins around the superficial layers (L1 and L2/3). (*C*) The PSDs of Z-score normalized fMRI time series (average of 40 voxels) showing the peaked low-frequency power at 0.01–0.02 Hz (purple arrows). (*D* and *E*) Average results ($n = 18$ trials of 4 rats) representing layer-wise intra- (*D*) and inter-laminar (*E*) lag times. (*D*) The middle layers (L2/3, 4, 5) show earlier lag times, whereas L6 shows significantly later lag times (one-way ANOVA, *posthoc: P-value < 0.05, Bonferroni correction). (*E*) In Ro-Mi, Mi-Ca, and Ro-Ca lag times, L2/3, 4, and 5 had earlier lag times (except L5 in Mi-Ca), whereas L1 (one-way ANOVA, *posthoc: P-value < 0.05, Bonferroni correction) and 6 (one-way ANOVA, ◆, ▲posthoc: P-value < 0.05, Bonferroni correction) had significantly later lag times, clearly showing the caudal to the rostral rs-fMRI signal propagation via L2/3 and L4.

shows the inter- and intra-laminar correlation maps of the rs-fMRI signals, presenting the highly correlated low-frequency signal fluctuation distributed in different cortical layers and across multipe cortical areas. In particular, the PSD analysis of the rs-fMRI signal fluctuation shows peaked oscillatory powers at 0.01–0.02 Hz across different cortial areas (Fig. 3C), which is consistent with the previous study in anesthetized rats (He et al. 2018). Based on intralaminar cross-correlation analysis, earlier lag times were detected in the middle layers (L2/3, 4, 5 median: −0.110, −0.180, −0.049 s), whereas significantly later lag times were detected in the deep layer (L6, median: 0.150 s) when compared to the mean BOLD signal of all the layers (Fig. 3D). To examine how the rs-fMRI signal propagated across different cortical areas, we calculated interlaminar lag times by comparing layer-wise BOLD signals between slices of Ro-Mi, Mi-Ca, and Ro-Ca (Fig. 3E). The lag times were not uniform across different layers. For the Ro-Ca case, it shows clear fMRI signal propagation from the caudal to the rostral slice at L2/3 and 4 (mean ± SEM: −0.869 ± 0.113 sec, −0.820 ± 0.120 s). Similarly, the Ro-Mi case shows earlier fMRI signal fluctuation at L2/3 to 6 from the middle to the rostral slice, but opposite at L1 (mean ± SEM: 0.033 ± 0.151 s), which may be caused by the large draining veins distributed across the middle slice (Fig. 3A). For the Mi-Ca case, the different lag time was only observed at L6, showing significantly later fMRI signal fluctuation at the caudal slice (mean ± SEM: 0.465 ± 0.088 s). The histograms of the permutation tests with laminar-specific time courses (e.g., L1 and L2/3, L1 and L4, etc.) of a representative trial (Fig. 3B, Supplementary Fig. S6) showed that the correlation values were statistically significant. Taken together, these results demonstrate resting-state laminar-specific temporal correlation features across different cortical

areas, which can be attributed to underlying either neuromodulation or vascular distribution across different cortical layers.

Discussion

In this study, we applied the MS-LS method to identify intra- and inter-laminar correlation patterns of evoked and resting-state fMRI signals with high spatial and temporal resolution across multiple cortical regions. Distinct laminar-specific correlation patterns in the cortex adjacent to the activated FP-S1 were detected based on either positive or negative BOLD responses, which may be regulated by altered brain states across different fMRI trials in anesthetized rats (Kobayashi et al. 2006; Devor et al. 2007; He et al. 2018; Wang et al. 2018; Parker and Razlighi 2019). The MS-LS mapping scheme is also applied to map the laminar correlation pattern of low frequency rs-fMRI signal fluctuation, presenting subsecond lag times of rs-fMRI signal propagation through cortical layers and across different cortical regions given the fast sampling rate.

An interesting observation of evoked laminar fMRI signal using the MS-LS method is the negative BOLD responses detected in the rostral region adjacent to FP-S1. Specifically, this temporal feature of the negative BOLD signal is different from the initial dip of positive BOLD as reported previously (Tian et al. 2010; Siero et al. 2015). It remains unclear whether the negative BOLD response has vascular or neuronal origins (Harel et al. 2002; Shmuel et al. 2002; Valabregue et al. 2003; Smith et al. 2004; Shmuel et al. 2006; Yacoub et al. 2006; Bressler et al. 2007; Pasley et al. 2007; Buxton 2010; Moraschi et al. 2012; Mullinger et al. 2014). As indicated by extensive studies, the BOLD signal relies on the integrated interactions of cerebral blood flow (CBF) and CBV changes with metabolic rate of oxygen consumption ($CMRO_2$) which are in principle caused by balanced proportional changes in both excitatory and inhibitory neuronal activity (Davis et al. 1998; Buxton et al. 2004; Logothetis 2008). Putative mechanisms of negative BOLD related to specific hemodynamic responses suggest two sources: i) the remaining elevation of CBV in contrast to returning to baseline CBF and $CMRO_2$ (Harel et al. 2002; Shmuel et al. 2002; Yacoub et al. 2006; Moraschi et al. 2012), and ii) the decoupling between CBF and $CMRO_2$ during or after stimulation (Valabregue et al. 2003; Yacoub et al. 2006; Buxton 2010). Also, based on the vascular blood supply, a local blood-stealing effect from adjacent cortices to provide more blood to the most activated region is also proposed (Smith et al. 2004; Bressler et al. 2007). With direct neuronal activity recording, the suppression of neuronal activity in the adjacent cortical regions due to lateral inhibition has also been reported (Shmuel et al. 2006; Pasley et al. 2007; Mullinger et al. 2014). The first two mechanisms (i and ii) for signal decrease below baseline following the BOLD activation profile are likely explained by the prolonged poststimulus undershoot in activated brain regions. As shown in Figure 2B, while the negative BOLD mainly occurred at the superficial layer where large arteries may contribute to CBV signal changes, robust negative BOLD signal was also detected at the L2/3 (blue color in the color bar). Also, the negative BOLD signal was maintained with longer spreading function than typical positive BOLD responses excluded the only contribution from CBV and CBF effects, suggesting a sustained corticocortical postsynaptic inhibition (see Supplementary Fig. S7A) (Butovas et al. 2006; Chen et al. 2020). It is also noteworthy that the negative BOLD group (group 2) shows the salient biphasic HRF of the positive BOLD, of which the poststimulus undershoot may be also caused by the decreased neuronal activity (Devor et al. 2007; Wang et al. 2018).

Using the MS-LS method, we also detected the robust rs-fMRI slow oscillation pattern across cortical layers of three slices with a peak frequency power at 0.01–0.02 Hz. Previous studies with simultaneous fMRI and optical fiber-based Ca^{2+} recording in anesthetized rats have reported that neuronal calcium oscillations underlie the low-frequency rs-fMRI signal fluctuation near 0.01–0.04 Hz (He et al. 2018). Also, intrinsic astrocytic Ca^{2+} transients have been reported to mediate global negative BOLD signals contributing to the low-frquency rs-fMRI signal fluctuation (Wang et al. 2018), suggesting brain state-dependent global neuromodulation of the ultraslow oscillatory patterns (Attwell et al. 2010; Petzold and Murthy 2011; Poskanzer and Yuste 2016). Moreover, negative global rs-fMRI during ultra-slow oscillation is also linked with pupil dynamics, showing converged effect of arousal state fluctuation and autonomus regulation (Bradley et al. 2008; Chang et al. 2016; Liu et al. 2018; Watson 2018; Ozbay et al. 2019; Pais-Roldan et al. 2020; Sobczak et al. 2021). In contrast to the brain-wide rs-fMRI mapping of previous studies, we revealed laminar-specific signal propagation of the low-frequency rs-fMRI signal fluctuation (Fig. 3E). Interestingly, the signal propagation direction varied at the different cortical layers. We observed more uniform lag times from L2/3 to L5 between different cortical regions, but largely varied lag times at L1 and L6. It is plausible that rs-fMRI signal oscillation in L2/3 to L5 is primarily driven by the global neuromodulation through subcortical projections (Constantinople and Bruno 2013), but the signal oscillation in L1 and L6 more likely relies on the different vascular density distribution that contributes to dynamic BOLD responses (Koopmans et al. 2010; Yu et al. 2012; Goense et al. 2016; Markuerkiaga et al. 2016; Schmid et al. 2019).

Technical limitations pertaining to MS-LS acquisition should be considered for future work. As a modification to the conventional line-scanning method (Yu et al. 2014), two saturation RF pulses were followed by three excitation RF pulses to acquire fMRI signals from three slices using MS-LS method. Given a certain set of sequence parameters (e.g., TE, readout bandwidth, etc.), imperfect performances of the saturation RF pulses result in contaminating fMRI signals, due to aliasing artifacts that

arise from fast T1 relaxation of tissue signals in outside of the FOV. It can be avoided by applying a ROI selective refocusing RF pulse (Mansfield et al. 1976; Finsterbusch and Frahm 2000; Choi et al. 2018) instead of saturation RF pulses. Moreover, in the interleaved acquisition of MS-LS, we have longer TR (100 ms in this work compared to 50 ms TR of the conventional method), thus preserving readout bandwidth due to tradeoff between tSNR enhancement and minimum TR. For the future work, implantable inductive coils (Chen et al. 2021; Inigo-Marco et al. 2021) or wireless amplified NMR detector (Qian et al. 2013; Qian et al. 2020) can be applied to enhance tSNR and to achieve a fast sampling rate simultaneously.

Supplementary Material

Supplementary material can be found at *Cerebral Cortex* online.

Author Contributions

X.Y. designed and supervised the research, H.Z. and X.Y. performed animal experiments, S.C., H.Z., and X.Y. acquired data, S.C. analyzed data, Y.C. and F.S. provided conceptual and technical support, X.Y., S.C., C.Q., and Y.C. wrote the manuscript.

Data Availability

The data that support the findings of this study are available from the corresponding authors upon request.

Code Availability

The related signal processing codes are available from the corresponding author upon reasonable request.

Funding

NIH Brain Initiative Funding (RF1NS113278-01, 1R01NS12 2904, NSF2123971); and the S10 Instrument Grant (S10 MH124733) to Martinos Center; German Research Foundation (DFG) (Yu215/3-1, BMBF 01GQ1702); and the internal funding from Max Planck Society. This project has received funding from the European Union Framework Programme for Research and Innovation Horizon 2020 (2014-2020) under the Marie Skłodowska-Curie Grant Agreement No. 896245. We thank Dr R. Pohmann, Dr J. Engelmann, Dr N. Avdievitch, and Ms H. Schulz for technical support, Dr P. Douay, Ms R. König, and Ms M. Pitscheider for animal support, the AFNI team for the software support.

Notes

Conflict of Interest: None declared.

References

Agrawal U, Brown EN, Lewis LD. 2020. Model-based physiological noise removal in fast fMRI. *NeuroImage*. 205:116231.

Albers F, Schmid F, Wachsmuth L, Faber C. 2018. Line scanning fMRI reveals earlier onset of optogenetically evoked BOLD response in rat somatosensory cortex as compared to sensory stimulation. *NeuroImage*. 164:144–154.

Attwell D, Buchan AM, Charpak S, Lauritzen M, MacVicar BA, Newman EA. 2010. Glial and neuronal control of brain blood flow. *Nature*. 468:232–243.

Balasubramanian M, Mulkern RV, Neil JJ, Maier SE, Polimeni JR. 2021. Probing in vivo cortical myeloarchitecture in humans via line-scan diffusion acquisitions at 7 T with 250-500 micron radial resolution. *Magnet Reson Med*. 85:42–55.

Bandettini PA, Jesmanowicz A, Wong EC, Hyde JS. 1993. Processing strategies for time-course data sets in functional MRI of the human brain. *Magn Reson Med*. 30:161–173.

Beckmann CF, DeLuca M, Devlin JT, Smith SM. 2005. Investigations into resting-state connectivity using independent component analysis. *Philos T R Soc B*. 360:1001–1013.

Birn RM, Diamond JB, Smith MA, Bandettini PA. 2006. Separating respiratory-variation-related fluctuations from neuronal-activity-related fluctuations in fMRI. *NeuroImage*. 31:1536–1548.

Biswal BB. 2012. Resting state fMRI: a personal history. *NeuroImage*. 62:938–944.

Biswal B, Yetkin FZ, Haughton VM, Hyde JS. 1995. Functional connectivity in the motor cortex of resting human brain using echo-planar MRI. *Magn Reson Med*. 34:537–541.

Biswal BB, Mennes M, Zuo XN, Gohel S, Kelly C, Smith SM, Beckmann CF, Adelstein JS, Buckner RL, Colcombe S et al. 2010. Toward discovery science of human brain function. *Proc Natl Acad Sci U S A*. 107:4734–4739.

Boorman L, Kennerley AJ, Johnston D, Jones M, Zheng Y, Redgrave P, Berwick J. 2010. Negative blood oxygen level dependence in the rat: a model for investigating the role of suppression in neurovascular coupling. *J Neurosci*. 30:4285–4294.

Bopp R, Holler-Rickauer S, Martin KAC, Schuhknecht GFP. 2017. An ultrastructural study of the thalamic input to layer 4 of primary motor and primary somatosensory cortex in the mouse. *J Neurosci*. 37:2435–2448.

Bradley MM, Miccoli L, Escrig MA, Lang PJ. 2008. The pupil as a measure of emotional arousal and autonomic activation. *Psychophysiology*. 45:602–607.

Bressler D, Spotswood N, Whitney D. 2007. Negative BOLD fMRI response in the visual cortex carries precise stimulus-specific information. *PLoS One*. 2:e410.

Buckner RL, Krienen FM, Yeo BT. 2013. Opportunities and limitations of intrinsic functional connectivity MRI. *Nat Neurosci*. 16:832–837.

Butovas S, Schwarz C. 2003. Spatiotemporal effects of microstimulation in rat neocortex: a parametric study using multielectrode recordings. *J Neurophysiol*. 90:3024–3039.

Butovas S, Hormuzdi SG, Monyer H, Schwarz C. 2006. Effects of electrically coupled inhibitory networks on local neuronal responses to intracortical microstimulation. *J Neurophysiol*. 96:1227–1236.

Buxton RB. 2010. Interpreting oxygenation-based neuroimaging signals: the importance and the challenge of understanding brain oxygen metabolism. *Front Neuroenerg*. 2:8.

Buxton RB, Uludag K, Dubowitz DJ, Liu TT. 2004. Modeling the hemodynamic response to brain activation. *NeuroImage*. 23:S220–S233.

Chang C, Leopold DA, Scholvinck ML, Mandelkow H, Picchioni D, Liu X, Ye FQ, Turchi JN, Duyn JH. 2016. Tracking brain arousal fluctuations with fMRI. *P Natl Acad Sci USA*. 113:4518–4523.

Chen Y, Sobczak F, Pais-Roldan P, Schwarz C, Koretsky AP, Yu X. 2020. Mapping the brain-wide network effects by optogenetic activation of the corpus callosum. *Cereb Cortex*. 30: 5885–5898.

Chen Y, Wang Q, Choi S, Zeng H, Takahashi K, Qian C, Yu X. 2021. Focal fMRI signal enhancement with implantable inductively coupled detectors. *NeuroImage* 247:118793.

Choi S, Zeng H, Pohmann R, Scheffler K, Yu X. 2018. Novel alpha-180 SE based LINE-scanning method (SELINE) for laminar-specific fMRI. *Proc Intl Soc Mag Reson Med*. 27:1166.

Choi S, Takahashi K, Jiang Y, Kohler S, Zeng H, Wang Q, Ma Y, Yu X. 2020. Real-time fMRI brain mapping in animals. *J Vis Exp*. 163:e61463.

Choi S, Chen Y, Zeng H, Biswal B, Yu X. 2021. Laminar-specific interhemispheric connectivity mapping with bilateral line-scanning fMRI. bioRxiv preprint. https://doi.org/10.1101/2021.03.08.433876.

Constantinople CM, Bruno RM. 2013. Deep cortical layers are activated directly by thalamus. *Science*. 340:1591–1594.

Cox RW. 1996. AFNI: software for analysis and visualization of functional magnetic resonance neuroimages. *Comput Biomed Res*. 29: 162–173.

Davis TL, Kwong KK, Weisskoff RM, Rosen BR. 1998. Calibrated functional MRI: Mapping the dynamics of oxidative metabolism. *Proc Natl Acad Sci USA*. 95:1834–1839.

Devor A, Tian P, Nishimura N, Teng IC, Hillman EM, Narayanan SN, Ulbert I, Boas DA, Kleinfeld D, Dale AM. 2007. Suppressed neuronal activity and concurrent arteriolar vasoconstriction may explain negative blood oxygenation level-dependent signal. *J Neurosci*. 27:4452–4459.

El-Boustani S, Sermet BS, Foustoukos G, Oram TB, Yizhar O, Petersen CCH. 2020. Anatomically and functionally distinct thalamocortical inputs to primary and secondary mouse whisker somatosensory cortices. *Nat Commun*. 11:3342.

Finn ES, Huber L, Jangraw DC, Molfese PJ, Bandettini PA. 2019. Layer-dependent activity in human prefrontal cortex during working memory. *Nat Neurosci*. 22:1687–1695.

Finsterbusch J, Frahm J. 2000. Gradient-echo line scan imaging using 2D-Selective RF excitation. *J Magn Reson*. 147:17–25.

Fox MD, Raichle ME. 2007. Spontaneous fluctuations in brain activity observed with functional magnetic resonance imaging. *Nat Rev Neurosci*. 8:700–711.

Friston KJ. 2011. Functional and effective connectivity: a review. *Brain Connect*. 1:13–36.

Gil R, Fernandes FF, Shemesh N. 2021. Neuroplasticity-driven timing modulations revealed by ultrafast functional magnetic resonance imaging. *NeuroImage*. 225:117446.

Goense JBM, Logothetis NK. 2006. Laminar specificity in monkey V1 using high-resolution SE-fMRI. *Magn Reson Imaging*. 24:381–392.

Goense J, Merkle H, Logothetis NK. 2012. High-resolution fMRI reveals laminar differences in neurovascular coupling between positive and negative BOLD responses. *Neuron*. 76:629–639.

Goense J, Bohraus Y, Logothetis NK. 2016. fMRI at high spatial resolution: implications for BOLD-models. *Front Comput Neurosc*. 10:66.

Harel N, Lee SP, Nagaoka T, Kim DS, Kim SG. 2002. Origin of negative blood oxygenation level-dependent fMRI signals. *J Cerebr Blood F Met*. 22:908–917.

He Y, Wang MS, Chen XM, Pohmann R, Polimeni JR, Scheffler K, Rosen BR, Kleinfeld D, Yu X. 2018. Ultra-slow single-vessel BOLD and CBV-based fMRI spatiotemporal dynamics and their correlation with neuronal intracellular calcium signals. *Neuron*. 97:925–939.

Hu X, Le TH, Ugurbil K. 1997. Evaluation of the early response in fMRI in individual subjects using short stimulus duration. *Magn Reson Med*. 37:877–884.

Huber L, Handwerker DA, Jangraw DC, Chen G, Hall A, Stuber C, Gonzalez-Castillo J, Ivanov D, Marrett S, Guidi M et al. 2017. High-resolution CBV-fMRI allows mapping of laminar activity and connectivity of cortical input and output in human M1. *Neuron*. 96:1253–1263.

Inigo-Marco I, Isturiz J, Fernandez M, Nicolas MJ, Dominguez P, Bastarrika G, Valencia M, Fernandez-Seara MA. 2021. Imaging of stroke in rodents using a clinical scanner and inductively coupled specially designed receiver coils. *Ann Biomed Eng*. 49: 746–756.

Jung WB, Shim HJ, Kim SG. 2019. Mouse BOLD fMRI at ultrahigh field detects somatosensory networks including thalamic nuclei. *NeuroImage*. 195:203–214.

Kashyap S, Ivanov D, Havlicek M, Sengupta S, Poser BA, Uludag K. 2018. Resolving laminar activation in human V1 using ultra-high spatial resolution fMRI at 7T. *Sci Rep-UK*. 8:17063.

Kim T, Masamoto K, Fukuda M, Vazquez A, Kim SG. 2010. Frequency-dependent neural activity, CBF, and BOLD fMRI to somatosensory stimuli in isoflurane-anesthetized rats. *NeuroImage*. 52: 224–233.

Kobayashi E, Bagshaw AP, Grova C, Dubeau F, Gotman J. 2006. Negative BOLD responses to epileptic spikes. *Hum Brain Mapp*. 27: 488–497.

Koopmans PJ, Barth M, Norris DG. 2010. Layer-specific BOLD activation in human V1. *Hum Brain Mapp*. 31:1297–1304.

Kunori N, Takashima I. 2016. High-order motor cortex in rats receives somatosensory inputs from the primary motor cortex via cortico-cortical pathways. *Eur J Neurosci*. 44:2925–2934.

Lewis LD, Setsompop K, Rosen BR, Polimeni JR. 2016. Fast fMRI can detect oscillatory neural activity in humans. *P Natl Acad Sci USA*. 113:E6679–E6685.

Liu X, de Zwart JA, Scholvinck ML, Chang CT, Ye FQ, Leopold DA, Duyn JH. 2018. Subcortical evidence for a contribution of arousal to fMRI studies of brain activity. *Nat Commun*. 9:395.

Logothetis NK. 2008. What we can do and what we cannot do with fMRI. *Nature*. 453:869–878.

Mansfield P, Maudsley AA, Baines T. 1976. Fast scan proton density imaging by NMR. *J Phys E Sci Instrum*. 9:271–278.

Markuerkiaga I, Barth M, Norris DG. 2016. A cortical vascular model for examining the specificity of the laminar BOLD signal. *NeuroImage*. 132:491–498.

Moraschi M, DiNuzzo M, Giove F. 2012. On the origin of sustained negative BOLD response. *J Neurophysiol*. 108:2339–2342.

Morgan AT, Nothnagel N, Petro LS, Goense J, Muckli L. 2020. High-resolution line-scanning reveals distinct visual response properties across human cortical layers. bioRxiv preprint. https://doi.org/10.1101/2020.06.30.179762.

Mullinger KJ, Mayhew SD, Bagshaw AP, Bowtell R, Francis ST. 2014. Evidence that the negative BOLD response is neuronal in origin: a simultaneous EEG-BOLD-CBF study in humans. *NeuroImage*. 94: 263–274.

Murphy K, Birn RM, Bandettini PA. 2013. Resting-state fMRI confounds and cleanup. *NeuroImage*. 80:349–359.

Nair G, Duong TQ. 2004. Echo-planar BOLD fMRI of mice on a narrow-bore 9.4 T magnet. *Magnet Reson Med*. 52:430–434.

Nunes D, Gil R, Shemesh N. 2021. A rapid-onset diffusion functional MRI signal reflects neuromorphological coupling dynamics. *NeuroImage*. 231:117862.

Ozbay PS, Chang C, Picchioni D, Mandelkow H, Chappel-Farley MG, van Gelderen P, de Zwart JA, Duyn J. 2019. Sympathetic activity contributes to the fMRI signal. *Commun Biol*. 2:421.

Pais-Roldan P, Biswal B, Scheffler K, Yu X. 2018. Identifying respiration-related aliasing artifacts in the rodent resting-state fMRI. *Front Neurosci*. 12:788.

Pais-Roldan P, Takahashi K, Sobczak F, Chen Y, Zhao X, Zeng H, Jiang Y, Yu X. 2020. Indexing brain state-dependent pupil dynamics with simultaneous fMRI and optical fiber calcium recording. *Proc Natl Acad Sci U S A*. 117:6875–6882.

Parker DB, Razlighi QR. 2019. Task-evoked negative BOLD response and functional connectivity in the default mode network are representative of two overlapping but separate neurophysiological processes. *Sci Rep*. 9:14473.

Pasley BN, Inglis BA, Freeman RD. 2007. Analysis of oxygen metabolism implies a neural origin for the negative BOLD response in human visual cortex. *NeuroImage*. 36:269–276.

Petzold GC, Murthy VN. 2011. Role of astrocytes in neurovascular coupling. *Neuron*. 71:782–797.

Poskanzer KE, Yuste R. 2016. Astrocytes regulate cortical state switching in vivo. *Proc Natl Acad Sci USA*. 113:E2675–E2684.

Preibisch C, Castrillon JG, Buhrer M, Riedl V. 2015. Evaluation of multiband EPI acquisitions for resting state fMRI. *PLoS One*. 10:e0136961.

Qian CQ, Yu X, Chen DY, Dodd S, Bouraoud N, Pothayee N, Chen Y, Beeman S, Bennett K, Murphy-Boesch J et al. 2013. Wireless amplified nuclear MR detector (WAND) for high-spatial-resolution mr imaging of internal organs: preclinical demonstration in a rodent model. *Radiology*. 268:228–236.

Qian W, Yu X, Qian CQ. 2020. Wireless reconfigurable RF detector array for focal and multiregional signal enhancement. *IEEE Access*. 8:136594–136604.

Raimondo L, Knapen T, Oliveira I, Yu X, van der Zwaag W, Siero J. 2019. Preliminary results of functional line-scanning in humans: submillimeter, subsecond resolution evoked responses. *Magn Reson Mater Phys Biol Med*. 32(Supplement 1):S22.06, p. S334.

de la Rosa N, Ress D, Taylor AJ, Kim JH. 2021. Retinotopic variations of the negative blood-oxygen-level dependent hemodynamic response function in human primary visual cortex. *J Neurophysiol*. 125:1045–1057.

Schmid F, Barrett MJP, Jenny P, Weber B. 2019. Vascular density and distribution in neocortex. *NeuroImage*. 197:792–805.

Sharoh D, van Mourik T, Bains LJ, Segaert K, Weber K, Hagoort P, Norris DG. 2019. Laminar specific fMRI reveals directed interactions in distributed networks during language processing. *Proc Natl Acad Sci USA*. 116:21185–21190.

Shmuel A, Yacoub E, Pfeuffer J, Van de Moortele PF, Adriany G, Hu XP, Ugurbil K. 2002. Sustained negative BOLD, blood flow and oxygen consumption response and its coupling to the positive response in the human brain. *Neuron*. 36:1195–1210.

Shmuel A, Augath M, Oeltermann A, Logothetis NK. 2006. Negative functional MRI response correlates with decreases in neuronal activity in monkey visual area V1. *Nat Neurosci*. 9: 569–577.

Siero JCW, Hendrikse J, Hoogduin H, Petridou N, Luijten P, Donahue MJ. 2015. Cortical depth dependence of the BOLD initial dip and poststimulus undershoot in human visual cortex at 7 Tesla. *Magnet Reson Med*. 73:2283–2295.

Siero J, Oliveira I, Choi S, Yu X. 2019. Implementing human line-scanning fMRI: initial results of ultra-high temporal and spatial resolution fMRI. *Proc Intl Soc Mag Reson Med*. 27:3933.

Silva AC, Koretsky AP. 2002. Laminar specificity of functional MRI onset times during somatosensory stimulation in rat. *Proc Natl Acad Sci U S A*. 99:15182–15187.

Silver NC, Dunlap WP. 1987. Averaging correlation-coefficients - should Fisher Z-transformation be used. *J Appl Psychol*. 72: 146–148.

Smith AT, Williams AL, Singh KD. 2004. Negative BOLD in the visual cortex: evidence against blood stealing. *Hum Brain Mapp*. 21: 213–220.

Smith SM, Fox PT, Miller KL, Glahn DC, Fox PM, Mackay CE, Filippini N, Watkins KE, Toro R, Laird AR et al. 2009. Correspondence of the brain's functional architecture during activation and rest. *Proc Natl Acad Sci USA*. 106:13040–13045.

Smith SM, Vidaurre D, Beckmann CF, Glasser MF, Jenkinson M, Miller KL, Nichols TE, Robinson EC, Salimi-Khorshidi G, Woolrich MW et al. 2013. Functional connectomics from resting-state fMRI. *Trends Cogn Sci*. 17:666–682.

Sobczak F, Pais-Roldan P, Takahashi K, Yu X. 2021. Decoding the brain state-dependent relationship between pupil dynamics and resting state fMRI signal fluctuation. *elife*. 10:e68980.

Thomson AM, Lamy C. 2007. Functional maps of neocortical local circuitry. *Front Neurosci*. 1:19–42.

Tian PF, Teng IC, May LD, Kurz R, Lu K, Scadeng M, Hillman EMC, De Crespigny AJ, D'Arceuil HE, Mandeville JB et al. 2010. Cortical depth-specific microvascular dilation underlies laminar differences in blood oxygenation level-dependent functional MRI signal. *Proc Natl Acad Sci USA*. 107:15246–15251.

Turner R, Le Bihan D, Moonen CT, Despres D, Frank J. 1991. Echo-planar time course MRI of cat brain oxygenation changes. *Magn Reson Med*. 22:159–166.

Valabregue R, Aubert A, Burger J, Bittoun T, Costalat R. 2003. Relation between cerebral blood flow and metabolism explained by a model of oxygen exchange. *J Cerebr Blood F Met*. 23:536–545.

Wang MS, He Y, Sejnowski TJ, Yu X. 2018. Brain-state dependent astrocytic Ca2+ signals are coupled to both positive and negative BOLD-fMRI signals. *Proc Natl Acad Sci USA*. 115:E1647–E1656.

Watson BO. 2018. Cognitive and physiologic impacts of the infraslow oscillation. *Front Syst Neurosci*. 12:44.

Yacoub E, Ugurbil K, Harel N. 2006. The spatial dependence of the poststimulus undershoot as revealed by high-resolution BOLD- and CBV-weighted fMRI. *J Cerebr Blood F Met*. 26:634–644.

Yeo BTT, Krienen FM, Sepulcre J, Sabuncu MR, Lashkari D, Hollinshead M, Roffman JL, Smoller JW, Zoller L, Polimeni JR et al. 2011. The organization of the human cerebral cortex estimated by intrinsic functional connectivity. *J Neurophysiol*. 106:1125–1165.

Yu X, Glen D, Wang S, Dodd S, Hirano Y, Saad Z, Reynolds R, Silva AC, Koretsky AP. 2012. Direct imaging of macrovascular and microvascular contributions to BOLD fMRI in layers IV-V of the rat whisker-barrel cortex. *NeuroImage*. 59:1451–1460.

Yu X, Qian C, Chen DY, Dodd SJ, Koretsky AP. 2014. Deciphering laminar-specific neural inputs with line-scanning fMRI. *Nat Methods*. 11:55–58.

Yu Y, Huber L, Yang J, Jangraw DC, Handwerker DA, Molfese PJ, Chen G, Ejima Y, Wu J, Bandettini PA. 2019. Layer-specific activation of sensory input and predictive feedback in the human primary somatosensory cortex. *Sci Adv*. 5:eaav9053.